2019

# Rational design of two-dimensional hybrid Co/N-doped carbon nanosheet arrays for efficient bi-functional electrocatalysis

Ningyan Cheng
*University of Wollongong*, nc174@uowmail.edu.au

Long Ren
*University of Wollongong*, lren@uow.edu.au

Gilberto Casillas
*University of Wollongong*, gilberto@uow.edu.au

Si Zhou
*University of Wollongong*, siz@uow.edu.au

Jincheng Zhuang
*Beihang University*, jincheng@uow.edu.au

***See next page for additional authors***

## Publication Details

Cheng, N., Ren, L., Casillas, G., Zhou, S., Zhuang, J., Wang, L., Xu, X., Dou, S. Xue. & Du, Y. (2019). Rational design of two-dimensional hybrid Co/N-doped carbon nanosheet arrays for efficient bi-functional electrocatalysis. Sustainable Energy and Fuels, 3 (7), 1757-1763.

# Rational design of two-dimensional hybrid Co/N-doped carbon nanosheet arrays for efficient bi-functional electrocatalysis

**Abstract**

Transition metals with desirable valence states have been proposed as efficient non-noble-metal electrocatalytic systems for selective water splitting. In this work, two-dimensional (2D) nitrogen-doped leaf-like carbon matrix arrays functionalized with multi-valence-state transition metal (cobalt) hybrids were successfully prepared by in situ calcination of the corresponding bimetallic leaf-like zeolitic imidazolate framework (ZIF-L) in an inert atmosphere. The 2D morphology of the matrix along with the particle size and surface valence state of the anchored particles has been successfully controlled via precisely adjusting the Co2+/(Zn2+ + Co2+) ratio in the bimetallic ZIF-L precursor. Electrochemical measurements show that the kinetics of and stability towards the hydrogen evolution reaction (HER) and oxygen evolution reaction (OER) are highly dependent on the particle size as well as the valence states. It was found that the particles with sizes less than 60 nm exhibit mixed Co0/Co2+ valence states, and therefore demonstrate bi-functional electrocatalytic performance. The theoretical simulations revealed that the bi-functional electrocatalytic activity should be attributed to the synergetic effect of mixed Co0/Co2+ and electronic coupling in the hybrids, which are of benefit to the catalytic kinetics and dynamics. High HER and OER activities of the hybrids have been verified, in which overpotentials of 171 and 280 mV to deliver a current density of 10 mA cm-2 for the HER and OER, respectively, were achieved. The obtained correlation between non-noble-metal-based carbon composites and HER/OER activities may be exploited as a rational guideline in the design and engineering of electrocatalysts.

**Disciplines**

Engineering | Physical Sciences and Mathematics

**Publication Details**

Cheng, N., Ren, L., Casillas, G., Zhou, S., Zhuang, J., Wang, L., Xu, X., Dou, S. Xue. & Du, Y. (2019). Rational design of two-dimensional hybrid Co/N-doped carbon nanosheet arrays for efficient bi-functional electrocatalysis. Sustainable Energy and Fuels, 3 (7), 1757-1763.

**Authors**

Ningyan Cheng, Long Ren, Gilberto Casillas, Si Zhou, Jincheng Zhuang, Li Wang, Xun Xu, Shi Xue Dou, and Yi Du

ARTICLE

# Rational Design of Two-Dimensional Hybrid Co/N-Doped Carbon Nanosheet Arrays for Efficient Bi-Functional Electrocatalysis

Received 00th January 20xx,
Accepted 00th January 20xx

DOI: 10.1039/x0xx00000x

Ningyan Cheng,[a] Long Ren,[a] Gilberto Casillas,[b] Si Zhou,[a] Jincheng Zhuang,[c] Li Wang,[d] Xun Xu,*[a] Shi Xue Dou[a,c] and Yi Du*[a,c]

Transition metals with desirable valence states have been proposed as efficient non-noble-metal electrocatalytic systems for selective water splitting. In this work, two-dimensional (2D) nitrogen-doped leaf-like carbon matrix arrays functionalized with multi-valence-state transition metal (cobalt) hybrids were successfully prepared by *in-situ* calcination of the corresponding bimetallic leaf-like zeolitic imidazolate framework (ZIF-L) in inert atmosphere. The 2D morphology of the matrix along with the particle size and surface valence state of the anchored particles has been successfully controlled via precise adjusting the $Co^{2+}/(Zn^{2+} + Co^{2+})$ ratio in the bimetallic ZIF-L precursor. Electrochemical measurements show that the kinetics and stability towards the hydrogen evolution reaction (HER) and oxygen evolution reaction (OER) are highly dependent on the particle size as well as their valence states. It was found that the particles with sizes less than 60 nm exhibit mixed $Co^0/Co^{+2}$ valence states, which demonstrate a bi-functional electrocatalytic performance. The theoretical simulations revealed that the bi-functional electrocatalytic activity should be attributed to the synergic effect of mixed $Co^0/Co^{+2}$ and electronic coupling in the hybrids, which are of benefit to the catalytic kinetics and dynamics. High HER and OER activities of the hybrids have been verified, in which an overpotential of 171 and 280 mV to deliver the current density of 10 $mA/cm^2$ for the HER and OER, respectively, were achieved. The obtained correlation between non-noble-metal-based carbon composites and HER/OER activities may be exploited as a rational guideline in the design and engineering of electrocatalysts.

## Introduction

Electrocatalytic water splitting, which has huge potential for economical green energy conversion, suffers from unaffordable costs and the limited supply of noble metals, which possess high activities toward the hydrogen evolution reaction (HER) and the oxygen evolution reaction (OER).[1,2] Great efforts have been devoted to develop effective and applicable non-noble-metal-based electrocatalysts.[1-5] Taking advantages of their high intrinsic electrocatalytic activities and earth abundance, 3*d* transition-metals (TMs, *e.g.*, Ni, Co, and Fe) are regarded as the most promising substitutes for noble metals in the HER and/or OER.[6-12] Unlike the noble metals, most 3*d* TMs possess various valence states arising from their *d*-orbitals, which are not fully occupied. This feature enables the 3*d* TMs to be used as electrocatalysts for both the HER and the OER, which is determined by the valence states. For example, the existence of Ni components with mixed valence states ($Ni^0$ and $Ni^{+2}$) enables Ni/NiO-nanofibers (NF) to possess bi-functional electrocatalytic activity towards water splitting.[13] In Ni/NiO-NF, $Ni^0$ is the HER active site while $Ni^{+2}$ is the source of the OER active site. Besides variable valence states, the distribution of TM-based particles on conductive supports also significantly affects their electrocatalytic activities.[10,14,15] An even distribution has been proven to effectively increase the surface active sites. The conductive supports can enhance charge transfer in electrocatalytic systems. Therefore, it is highly desirable to develop the 3*d* TM-based electrocatalysts, which possess variable valence states and exhibit even dispersions on their conductive supports.

Using an annealing process is the general approach to achieve 3*d* TM-based electrocatalysts with variable valence states. By precisely controlling the annealing conditions, mixed valence states can be modulated accurately within the 3*d* TM-based electrocatalysts, which, in turn, facilitates the synthesis of multifunctional TM-based electrocatalysts. Nevertheless, it is hard to avoid particle aggregation in annealing, which decreases the density of active surface sites.[15-17] Wet-chemical routes, such as the hydrothermal method, on the other hand, can suppress the aggregation by controlling particle dispersion, but face difficulties in modulating valence states. Thus, it is still extremely challenging to synthesize well-distributed TM particles with controllable mixed valence states on conductive supports for electrocatalysis, which is very much in demand for the development of multi-functional TM-based electrocatalysts.

In this work, we designed and successfully synthesized valence-state controllable Co based nanoparticles in 2D nitrogen-doped leaf-like

[a] *Institute for Superconducting and Electronic Materials (ISEM), Australian Institute for Innovative Materials (AIIM), University of Wollongong, Wollongong, NSW 2500, Australia. E-mail: ydu@uow.edu.au; xun@uow.edu.au*
[b] *Electron Microscopy Centre (EMC), Australian Institute for Innovative Materials (AIIM), University of Wollongong, Wollongong, NSW 2500, Australia.*
[c] *BUAA-UOW Joint Research Centre and school of Physics, Beihang University, Beijing, 10191, P. R. China.*
[d] *School of Chemistry, Monash University, Clayton, Victoria, 3800 Australia.*
Electronic Supplementary Information (ESI) available: [details of any supplementary information available should be included here]. See DOI: 10.1039/x0xx00000x

carbon matrix arrays on conductive carbon cloth (CoNC-*x*/CC, where *x* is the ratio of $Co^{2+}/(Zn^{2+} + Co^{2+})$ in the precursor), which was derived from bimetallic leaf-like zeolitic imidazolate framework nanosheet arrays (BMZIF-*x*/CC, where *x* is the ratio of $Co^{2+}/(Zn^{2+} + Co^{2+})$ in the precursor). The distance between adjacent $Co^{2+}$ ions in BMZIF-*x*/CC, which determines the valence states and distribution of the Co based particles in CoNC-*x*/CC, is mainly controlled by the value of *x*. Meanwhile, the 2D-type ZIF matrix maximizes exposure of the functional particles on the surface after pyrolysis, which helps to fully exploit the catalytic activity of the Co with a desirable valence state. It was found that the obtained 2D CoNC-*x*/CC (*x* = 0.5, 0.625, 0.75, and 0.875) with uniformly dispersed cobalt-based particles and possessing mixed valence states of $Co^0$ and $Co^{+2}$ as the surface active sites, has high bi-functional electrocatalytic performance. The typical CoNC-0.75/CC only needs overpotentials ($\eta$) of 171 and 280 mV to deliver 10 mA/cm$^2$ for the HER and OER in 1.0 M KOH, respectively, and this high catalytic activity can be maintained for at least 40 hours. Theoretical calculations were also performed, and the results further explained and confirmed these experimental observations.

## Experimental

$Co(NO_3)_2{\cdot}6H_2O$, $Zn(NO_3)_2{\cdot}H_2O$, 2-methylimidazole, KOH, and Nafion (5 wt%) were purchased from Sigma-Aldrich. All chemicals were used as received without any further purification. Carbon cloth (CC) was provided by Hongshan District, Wuhan Instrument Surgical Instruments. The water used throughout all the experiments was purified through a Millipore system.

**Preparation of BMZIF-x/CC**

In a typical synthesis, 0.4 × *x* (*x* = 0, 0.25, 0.5, 0.625, 0.75, 0.875, 1) mmol $Co(NO_3)_2{\cdot}6H_2O$ and 0.4 × (1-*x*) mmol $Zn(NO_3)_2{\cdot}H_2O$ were dissolved in 4 mL of deionized water to form the clear solution A. Similarly, 0.13 g of 2-methylimidazole was dissolved in 4 ml deionized water to form solution B. Then, solution A was quickly poured into solution B, and then a piece of CC, which was sequentially cleaned by sonication in acetone, water, and ethanol for 30 min each, was immediately immersed in the above mixed solution. After 2 hours of reaction, the CC was taken out and washed with deionized water and dried at 60 °C.

**Preparation of CoNC-x/CC**

The BMZIF-*x*/CC was placed in a ceramic crucible with a cover and then calcined at 800 °C for 1 h at a ramp rate of 5 °C/min under $N_2$ atmosphere. The obtained materials were used without any further treatment.

**Characterization**

Scanning electron microscopy (SEM) images were collected on a JEOL JSM-7500FA scanning electron microscope. Transmission electron microscope (TEM) images were collected on a JEOL JEM-2010 electron microscope operated at 200 kV. High resolution scanning TEM (STEM) images, and STEM-energy dispersive X-ray spectroscopy (EDX) images were obtained using a JEOL ARM-200CF operated at 200 kV with an X-ray collection angle of ~1 sr. The EDX elemental mapping was obtained using NSS 3.3.94 Noran System Seven software, in which principal component analysis can be performed to identify regions with a similar composition within a map. Powder X-ray diffraction (XRD) patterns were collected using MAC Science.

Electrochemical measurements

Electrochemical measurements were performed with a Bio Logic Science Instruments VSP-300 electrochemistry workstation. All the electrochemical measurements were conducted in a typical three-electrode setup with an electrolyte solution of 1.0 M KOH using CC and CoNC-*x*/CC directly as the working electrode, a graphite rod as the counter electrode, and saturated calomel electrode (SCE) as the reference electrode. In all measurements, the SCE reference electrode was calibrated with respect to reversible hydrogen electrode (RHE). Linear sweep voltammetry (LSV) measurements were conducted at scan rates of 2 mV/s and 5 mV/s for the hydrogen evolution reaction (HER) and the oxygen evolution reaction (OER), respectively. All the potentials reported in our work are vs. SCE in 1.0 M KOH. $E$ (RHE) = $E$ (SCE) + 0.059 pH + 0.242. For the OER, the overpotential ($\eta$) = $E$ (RHE) - 1.23 V. The calculation of current density was based on the geometrical area. All the data are presented without *iR* compensation.

**Computational methods**

Spin-polarized density functional theory (DFT) calculations were performed with the Vienna ab initio simulation package (VASP),[18] using the planewave basis with an energy cutoff of 500 eV, projector augmented wave pseudopotentials,[19] and the generalized gradient approximation parameterized by Perdew, Burke and Ernzerhof (GGA-PBE) for the exchange-correlation functional.[20] Solids of Co in the face-centered cubic (fcc) phase, CoO, $RuO_2$ (110), and Pt (111) were modeled by four-layer slabs, with 2 × 2 unit cells for the lateral dimensions of the supercells. Both (111) and (100) surfaces were considered for Co and CoO. The NG@Co heterostructure was modeled by a supercell consisting of 4 × 4 unit cells for graphene on a Co (111) surface. The in-plane lattice of Co was slightly compressed to fit that of graphene, giving a lattice mismatch of 1.99%. Then, one N atom was substituted into the graphene sheet, corresponding to a doping concentration of 3.12 at.%. For all the models, a vacuum space 16 Å in thickness was applied in the vertical direction. The Brillouin zones of the supercells were sampled by a uniform **k** point mesh with density higher than 0.03 Å$^{-1}$. With fixed cell parameters, the model structures were fully optimized using the convergence criteria of $10^{-4}$ eV for the electronic energy and $10^{-2}$ eV/Å for the forces on each atom. The bottom-layer atoms were fixed during structure relaxation to mimic semi-infinite solids. Grimme's semi-empirical DFT-D3 scheme for dispersion correction was adopted to describe the van der Waals (vdW) interactions in layered materials.[21] The climbing-image nudged elastic band (CI-NEB) method was employed to determine the kinetic barriers and transition states for the water dissociation process.[22] Five images were used to mimic the reaction path. The intermediate images were relaxed until the perpendicular forces were less than $10^{-2}$ eV/ Å.

## Results and discussion

As illustrated in Fig. 1a and Fig. S1 and S2 in the Supporting Information, a series of BMZIF-*x*/CC samples were synthesized by a simple hydrothermal method at room temperature. Their X-ray diffraction (XRD) patterns (Fig. S3), Fourier-transform infrared (FTIR)

spectra (Fig. S4), and Raman spectra (Fig. S5) are consistent with the reported data on the bimetallic leaf-like zeolitic imidazolate framework precursor (ZIF-L).[23-26] This confirms that the as-prepared BMZIF-*x*/CC can be assigned to ZIF-L, regardless of the value of *x*. A distinct morphological evolution was observed during the calcination process. After calcination, the 2D leaf-like nanosheet arrays of CoNC-*x*/CC (*x* = 0.5, 0.625, 0.75, 0.875, and 1) retained their 2D structures with nanoparticles attached on the surface (Fig. S6**)**. The particle size increases along with the value of *x*. In contrast, the BMZIF-*x*/CC samples with *x* = 0 and 0.25 lose their 2D features and fully collapse after calcination, as shown in Fig. S6. We believe that the collapse gives rise to the carbonization of the ZIF framework as well as evaporation of Zn at high calcining temperatures.[27] As shown in Fig. 1b, the XRD patterns of the CoNC-*x*/CC (*x*= 0 and 0.25) samples only correspond to graphite carbon, while the rest of the samples (*x* = 0.5, 0.625, 0.75, 0.875, and 1) possess additional XRD peaks assigned to metallic Co. The four Raman-active peaks located at 182, 459, 500, and 654 $cm^{-1}$, as shown in Fig. 1c, verify that CoO also exists in the CoNC-*x*/CC (*x* = 0.5, 0.625, 0.75, 0.875, and 1) samples.[28] The coexistence of metallic Co and CoO in CoNC-*x*/CC (*x* = 0.5, 0.625, 0.75, 0.875, and 1) is unlike what appears in the samples with *x*= 0 and 0.25, which suggests that the valence state of the Co component in CoNC-*x*/CC can be modulated by the value of *x*.

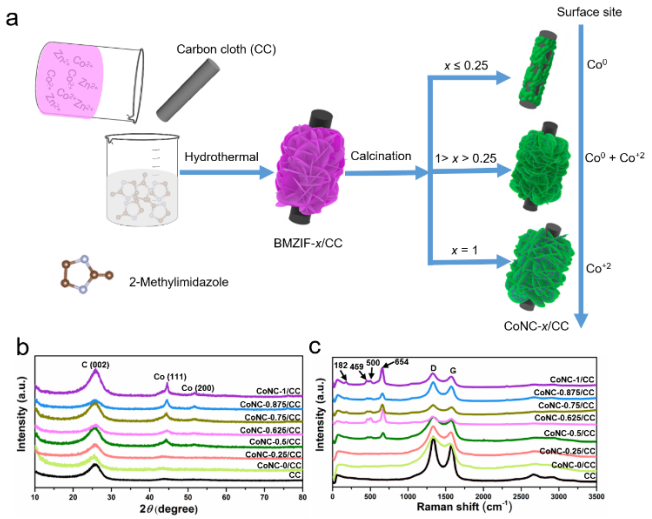


**Fig. 1** (a) Schematic diagram illustrating the structure and configuration of BMZIF-*x*/CC and the corresponding CoNC-*x*/CC obtained after pyrolysis; (b) XRD patterns, and (c) Raman spectra of the CC and CoNC-*x*/CC.

In order to further reveal the role of *x* in manipulating the terminated surface active valence state of the Co component and the morphology of the samples, we carried out scanning transmission electron microscopy (STEM) on CoNC-*x* (scratched from CoNC-*x*/CC). The backscattered electron microscopy image and STEM images (Fig. S7) show that there are very few particles embedded in the collapsed CoNC-0.25. The high resolution image of the particle (inset of Fig. S7d) reveal that it possesses an interplanar distance of 0.206 nm, corresponding to the (111) crystal plane of metallic Co. The above results agree well with negligible signal of Co components in the XRD and Raman results. In contrast, the 2D CoNC-*x* (*x* = 0.5, 0.625, 0.75, 0.875, and 1) samples possess significant amounts of nanoparticles with an even distribution, as shown in Fig. S8. Moreover, increasing *x* results in an increase in the particle size. Interestingly, the valence state of cobalt also varies, depending on the particle size. The high-angle annular dark-field STEM (HAADF-STEM) image and corresponded energy dispersive X-ray (EDX) spectrum and elemental maps of a 2D CoNC-0.75 nanosheet (Fig. 2b-2f and Fig. S9), which was scratched from a typical CoNC-*x*/CC (*x* = 0.75) sample (Fig. 2a), reveals the existence and uniform dispersion of C and N. The HAADF-STEM images of a selected small particle ~7 nm in size (Fig. 2g and 2h, and Fig. S10) show that it is a pure metallic Co particle covered by a graphitic layer, which is believed to prevent the metallic Co from being oxidized during annealing. In a large particle (~70 nm), the covering layer of Co is distinct from the graphitic layers of the small particles. The phase mapping (Fig. S11) reveals that this is a CoO shell, which is also confirmed by the semi-coherence between Co and CoO down the [011] zone axis in interface of the HAADF-STEM images (Fig. 2i). The particles 50 nm in size show the both features of both small and large particles, that is, the Co core is covered by a shell consisting of graphitized carbon and CoO, as shown in Fig. 2j-l. Thus, the valence states of cobalt in CoNC-*x*/CC can be tuned by the sizes of the nanoparticles, which is determined by the ratio *x* of $Co^{2+}/(Zn^{2+} + Co^{2+})$ in the precursor.

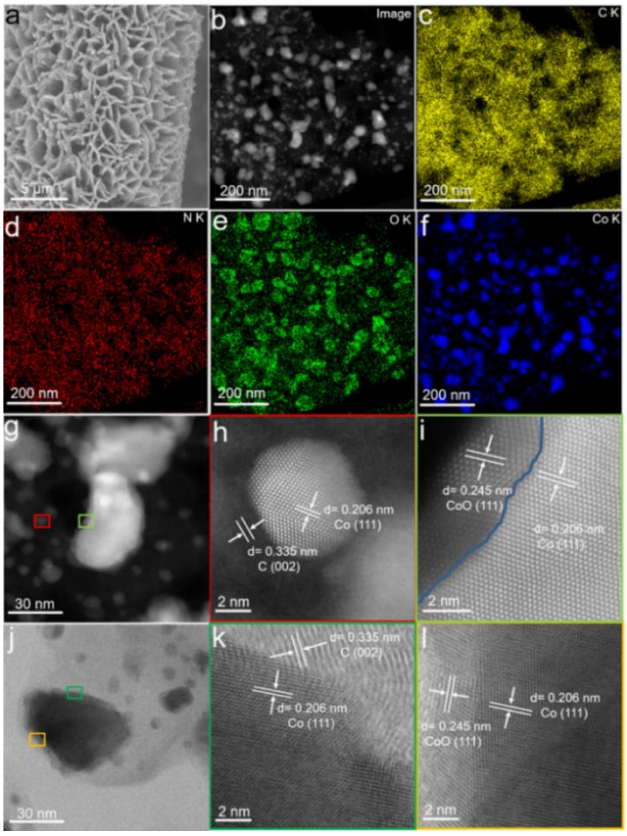


**Fig. 2** (a) Scanning electron microscope image of CoNC-0.75/CC; (b) HAADF-STEM image and (c, d, e, f) EDX elemental mapping analysis of a CoNC-0.75 sample scratched from CoNC-0.75/CC; (g) HAADF-STEM image of a selected small area of the CoNC-0.75; (h) High magnification HAADF-STEM image of the selected small particle in (g) marked by the red rectangle; (i) High magnification HAADF-STEM image of the selected small area of the large particle in (g) marked by the light green rectangle, with the blue line indicating the interface. (j) BF-STEM image of another selected small area of the CoNC-0.75; (k) High magnification BF-STEM images of the selected part of the particle in (j) marked by the green rectangle; (l) High magnification BF-STEM images of the selected part of the particle in (j) marked by the orange rectangle.

Considering that $Co^0$ is usually the source of HER active sites while $Co^{+2}$ is the source of OER active sites, the coexistence of $Co^0$ and $Co^{+2}$

as terminated surface sites may offer CoNC-*x* bi-functional elecrocatalytic activity. To verify this hypothesis, electrocatalytic HER and OER activities over CoNC-*x*/CC were evaluated in 1.0 M KOH aqueous solution by using a standard three-electrode system. For comparison, the electrocatalytic activity of CC was also examined. The polarization curves in Fig. 3a show that blank CC exhibits negligible HER activity. Though possessing a similar collapsed structure, to reach the current density of 10 mA/cm$^2$, the overpotential required by CoNC-0.25/CC (256 mV) is notably lower than that of cobalt metal-free CoNC-0/CC (444 mV). Meanwhile, the overpotentials required for CoNC-0.5/CC, CoNC-0.625/CC, CoNC-0.75/CC, CoNC-0.875/CC, and CoNC-1/CC with retained 2D leaf-like structure are only 194, 188, 171, 168, and 195 mV, respectively. To reach the high current density of 100 mA/cm$^2$, CoNC-0.5/CC, CoNC-0.625/CC, CoNC-0.75/CC, and CoNC-0.875/CC need 626, 589, 577, 606, and 657 mV, respectively. Thus, it is clear that CoNC-*x*/CC (*x* = 0.5, 0.625, 0.75, and 0.875), which contain mixed valence state Co based particles, exhibit very similar catalytic activity, but it is obviously higher than that of CoNC-*x*/CC (*x* = 0, 0.25, and 1). The catalytic activity of the as-prepared catalysts also compares favorably with the behavior of most recently reported cobalt and cobalt oxide based electrocatalysts, as summarized in Table S1. Tafel slop is commonly used to determine the reaction kinetics and rate-determining step in HER. It is established that the Tafel slopes are about 30, 40, 120 mV/dec for the Tafel, Heyrovsky, and Volmer reaction mechanism in the HER, respectively.[29-32] Since the Tafel slop of the CoNC-*x*/CC is higher than 110 mV/dec (Fig. S12a), therefore, it suggests that the rate-determining step here is the electrochemical desorption, and the Volmer-Heyrovsky mechanism applies for towards HER. Since long-term stability is another critical parameter in determining the practical capability of an electrocatalyst, a stability test of the typical CoNC-0.75/CC was also performed. The long stability of CoNC-0.75/CC was confirmed by the negligible difference between the polarization curves obtained before and after continuous cyclic voltammetry (CV) scanning for 1000 cycles, and the time-dependent current density curve under the static overpotential of 170 mV (Fig. 3b).

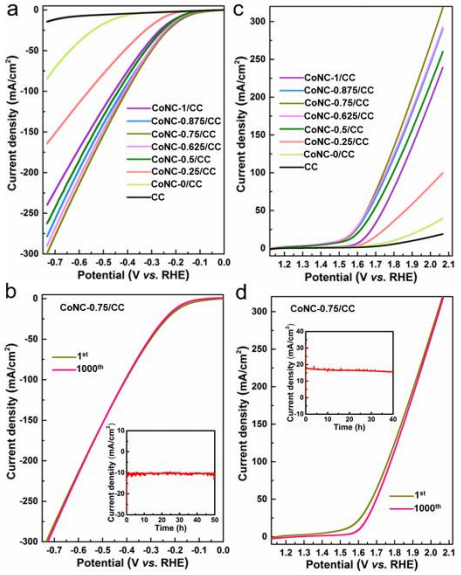


**Fig. 3** (a) HER polarization curves of CoNC-*x*/CC (*x* = 0, 0.25, 0.5, 0.625, 0.75, 0.875, 1); (b) HER polarization curves of CoNC-0.75/CC initially and after 1000 cyclic voltammetry (CV) scans at a scan rate of 100 mV/s (inset: time-dependent current density curve of CoNC-0.75/CC under a static overpotential of 170 mV for 50 h). (c) OER polarization curves of CoNC-*x*/CC (*x* = 0, 0.25, 0.5, 0.625, 0.75, 0.875; 1), (d) OER polarization curves of CoNC-0.75/CC initially and after 1000 CV scans at a scan rate of 100 mV/s (inset: time-dependent current density curve of CoNC-0.75/CC under a static overpotential of 340 mV for 40 h).

Moreover, after the stability test, SEM images show that CoNC-0.75/CC still retains its 2D nanosheet arrays without collapse (Fig. S13a and S13b). The XRD pattern (Fig. S13c) collected after the test is also similar with the one obtained before test, and only peaks attributed to graphitic carbon and metallic Co could be found. Therefore, all the data show there is no obvious change on the morphology and composition of the sample after the stability test, which further confirms the high stability of the sample.

The electrocatalytic OER activity of CC and the series of CoNC-*x*/CC samples was also evaluated under the same test conditions. Similar to the case of the HER, Fig. 3c shows that CC possesses negligible catalytic activity towards the OER. To achieve current density of 10 mA/cm$^2$, the overpotential required for CoNC-0/CC and CoNC-0.25/CC was 567 and 434 mV, respectively, which are much higher than those of CoNC-0.5/CC (307 mV), CoNC-0.625/CC (265 mV), CoNC-0.75/CC (280 mV), CoNC-0.875/CC (279 mV), and CoNC-1/CC (392 mV). The samples (CoNC-*x*/CC, *x* = 0.5, 0.625, 0.75, and 0.875) which retain the 2D structure and contain mixed valence-state type Co-based particles, exhibit very similar OER catalytic activity and Tafel slopes (Fig. S12b), which demonstrate identical catalytic mechanism. However, their catalytic activity is superior to that of CoNC-*x*/CC (*x* = 0, 0.25, and 1). As summarized in Table S2, the OER activity of the typical CoNC-0.75/CC is comparable to those of many outstanding cobalt-based electrocatalysts. The catalytic OER stability of CoNC-0.75/CC was also evaluated by comparing the polarization curves before and after continuous CV scanning for 1000 cycles (as shown in Fig. 3d), and no obvious difference was observed. The time-dependent current density curve under a static overpotential of 340 mV for 40 h further demonstrates that CoNC-0.75/CC possesses high electrocatalytic stability. As shown in Fig. S14, the high stability of the sample was also confirmed by the fact that there is no obvious change in the morphology and composition before and after the long-time stability test.

To gain insight on the atomic level into the origins of the bi-functional activity of the CoNC-*x* composites, density functional theory calculations were performed to examine the electrocatalytic properties of different components in the composites. As shown in Fig. 4a and Fig. S15, we consider the Co (111) surface covered by an N-doped graphene monolayer to mimic the sample region where Co nanoparticles are embedded in N-doped graphitic carbon shells (denoted by NG@Co). We use bared Co and CoO solids to model the regions where graphitic sheets rupture and Co nanoparticles are exposed and (partially) oxidized into CoO. Besides the (111) surface, which is the dominant exposed surface of Co based nanoparticles according to the experimental transmission electron microscope (TEM) and STEM images, the (100) surface was also examined. The OER overpotentials ($\eta^{OER}$) of these model structures were calculated by the standard hydrogen electrode method, considering the four electron pathway in alkaline medium.[33] The HER activity was characterized by the Gibbs free energy for H* adsorption ($\Delta G_{H^*}$),[34]

and the kinetic barrier for water to dissociate into $H^+$ and $OH^-$ ions. The details of the computational method can be found elsewhere.[33-36] In general, an ideal bi-functional OER and HER catalyst has $\eta^{OER}$ and $\Delta G_{H^*}$ equal to zero, requiring that the catalyst can provide moderate binding strength for the reaction intermediates (O*, OH*, OOH* and H* species) to minimize the potential barriers between consecutive reaction steps.[37] Catalysts for the HER in an alkaline medium are also expected to facilitate water dissociation.

Fig. 4b, 4c displays the free energy diagrams of the OER and HER for different model structures. Overall, the N-doped graphene supported by the Co (111) surface exhibits high electrocatalytic activity towards both the OER and the HER. The OER overpotential required is as low as 0.44 V, comparable to that of $RuO_2$ (0.40 V for the (110) surface). The most active sites come from the C atoms in the para-position with respect to the N dopant and on the hollow sites of the Co (111) surface. The bare CoO (100) surface also shows activity towards the OER with Co serving as the reaction sites and giving $\eta^{OER}$ = 0.50 V. For both model structures, the formation of OOH* intermediate from O* and $OH^-$ species is the rate-limiting step. For the HER, the C atoms next to the N dopant in the Co supported graphitic sheet have $\Delta G_{H^*}$ = 0.13 eV, which is most competitive to that of Pt (-0.09 eV for the (111) surface). The bare Co (111) and (100) surfaces provide too strong and too weak H* binding for HER catalysis, with $\Delta G_{H^*}$ = -0.48 and 0.24 eV, respectively. In comparison, free-standing N-doped graphene (denoted by NG) has much weaker binding capability than the graphene supported by Co metal, and consequently, it has lower OER activity and is ineligible for HER catalysis. The detailed catalytic performances of various model structures are given by Table S3. The synergic effects of heterostructures of graphitic carbon materials and transition metals is attributed to the interfacial electronic coupling, which has been well elucidated by previously reported theoretical work.[35, 36]

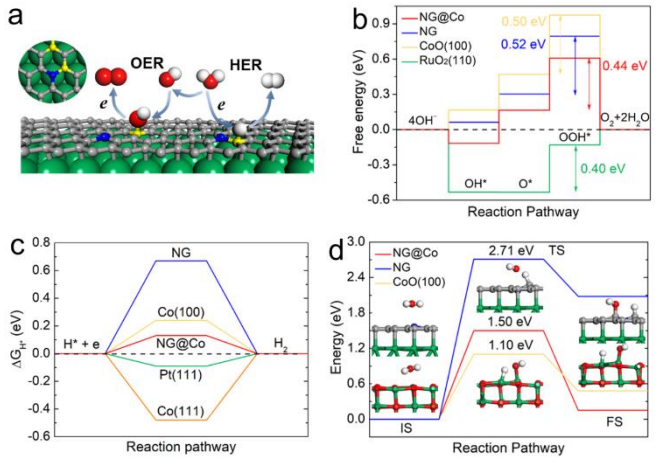


**Fig. 4** (a) Model structure of N-doped graphene supported by Co (111) surface, and schematic illustration of the OER and HER on the active sites (highlighted in yellow). (b) Free energy diagrams of the OER at pH = 14 and $T$ = 298 K at the equilibrium potential ($U_0$ = 0.402 V) for various model systems; the double-headed arrows and the numbers next to them indicate the rate-limiting steps and OER overpotentials, respectively. (c) Free energy diagrams for hydrogen evolution at zero potential for various model systems. The black dashed lines in (b) and (c) indicate the ideal free energies for OER and HER catalysis, respectively. (d) Reaction energy diagram of water dissociation on NG@Co (red line), CoO (100) (yellow line), and NG (blue line). The insets show the side-view structures of the initial states (IS), transition states (TS), and final states (FS) for NG@Co and CoO(100), respectively. The numbers indicate the kinetic barriers to water dissociation. The H, C, N, O, and Co atoms are shown in white, grey, blue, red, and green, respectively.

Moreover, the dissociation of water molecules is facile on N-doped graphene supported by the Co (111) surface, involving a barrier of 1.50 eV, comparable to that of Pt (0.89 eV),[38] and much lower than the value for free-standing N-doped graphene (2.71 eV). Exposure of the CoO (100) surface, which is hydrophilic, can further promote water dissociation, with a barrier of only 1.10 eV, as shown by Fig. 4d. Our calculations reveal that the synergic effects between Co nanoparticles, N-doped graphitic sheets, and the oxidized Co surfaces, endow the hybrid material with bi-functional activities towards the OER and HER, with different reaction sites for the two processes, as illustrated by Fig. 4a. Partial exposure of the CoO (100) surface can provide more reaction sites for the OER and water dissociation, and thus enhance the bi-catalytic performance. These theoretical results are well consistent with the experimental observations that the CoNC-*x* composites with the coexistence of both $Co^0$ and $Co^{+2}$ states have the best bi-functional performance, better than either pure $Co^0$ or pure $Co^{+2}$.

## Conclusions

In conclusion, Co-based CoNC-*x*/CC nanosheet arrays with controllable valence states of Co, tunable particle size, and precise nanoparticle distributions have been successfully synthesized. The valence states and the distribution of the Co based particles in CoNC-*x*/CC were determined by the distance between adjacent $Co^{2+}$ ions in BMZIF-*x*/CC, which can be controlled by precisely adjusting the ratio of $Co^{2+}/(Zn^{2+} + Co^{2+})$ in the precursor. It was found that the particles with sizes less than 60 nm exhibited mixed $Co^0/Co^{+2}$ valence states, so that they demonstrate a bi-functional electrocatalytic performance. The theoretical simulations confirm that bi-functional electrocatalytic activity is attributable to the synergic effects of mixed $Co^0/Co^{+2}$ and the electronic coupling in the hybrids, which are of benefit to the catalytic kinetics and dynamics. High HER and OER activities of the hybrids have been demonstrated. The obtained correlation between non-noble-metal-based carbon composites and HER/OER activities offers a simple route to design and engineer hybrid systems for bi-functional electrocatalysis.

## Conflicts of interest

There are no conflicts to declare.

## Acknowledgements

This work was financially supported by the Australian Research Council (DP160102627, DP170101467, and FT180100585), the National Natural Science Foundation of China (11874003), and a BUAA-UOW Joint Research Centre Small Grant. The authors acknowledge the use of the facilities at the UOW Electron Microscopy Centre funded by ARC grants (LE0882813 and LE120100104). The authors thank T. Silver for valuable comments.

## References


1. T. Ma, S. Dai and S. Qiao, *Mater. Today,* 2016, **19**, 265.
2. Y. Jiao, Y. Zheng, M. Jaroniec and S. Qiao, *Chem. Soc. Rev.*, 2015, **44**, 2060.
3. Y. Zhu, C. Guo, Y. Zheng and S. Qiao, *Acc. Chem. Res.,* 2017, **50**, 915.
4. Y. Yan, B. Xia, B. Zhao and X. Wang, *J. Mater. Chem. A,* 2016, **4**, 17587.
5. X. Zou and Y. Zhang, *Chem. Soc. Rev*., 2015, **44**, 5148.
6. J. Wang, H. Zhang and X. Wang, *Small,* 2017, **1**, 1700118.
7. L. Han, S. Dong and E. Wang, *Adv. Mater.,* 2016, **28**, 9266.
8. M. Gong, D. Wang, C. Chen, B. -J. Hwang and H. Dai, *Nano Research,* 2016, **9**, 28.
9. F. Lu, M. Zhou, Y. Zhou and X. Zeng, *Small,* 2017, **13**, 1701931.
10. S. Chen, J. Duan, J. Ran, M. Jaroniec and S. Qiao, *Energy Environ. Sci.,* 2013, **6**, 3693.
11. J. Gao, N. Ma, Y. Zheng, J. Zhang, J. Gui, C. Guo, H. An, X. Tan, Z. Yin and D. Ma, *ChemCatChem,* 2017, **9**, 1601.
12. Y. Shi, Y. Wang, Y. Yu, Z. Niu and B. Zhang, *J. Mater. Chem. A,* 2017, **5**, 8897.
13. X. Han, Y. Yu, Y. Huang, D. Liu and B. Zhang, *ACS Catal.,* 2017, **7**, 6464.
14. H. Jin, J. Wang, D. Su, Z. Wei, Z. Pang and Y. Wang, *J. Am. Chem. Soc.,* 2015, **137**, 2688.
15. M. Gong, W. Zhou, M. -C. Tsai, J. Zhou, M. Guan, M. -C. Lin, B. Zhang, Y. Hu, D. Wang, J. Yang, S. J. Pennycook, B. -J. Hwang and H. Dai, *Nat. Commun.*, 2014, **5**, 4695.
16. X. Zhu, M. Liu, Y. Liu, R. Chen, Z. Nie, J. Li and S. Yao, *J. Mater. Chem. A,* 2016, **4**, 8974.
17. A. J. Esswein, M. J. McMurdo, P. N. Ross, A. T. Bell and T. D. Tilley, *J. Phys. Chem. C,* 2009, **113**, 15068.
18. G. Kresse and J. Furthmüller, *Phys. Rev. B*, 1996, **54**, 11169.
19. G. Kresse and D. Joubert, *Phys. Rev. B,* 1999, **59**, 1758.
20. J. P. Perdew, K. Burke and M. Ernzerhof, *Phys. Rev. Lett.,* 1996, **77**, 3865.
21. S. Grimme, J. Antony, S. Ehrlich and H. Krieg, *J. Chem. Phys.,* 2010, **132**, 154104.
22. G. Henkelman, B.P. Uberuaga, H. Jónsson and G**.** Henkelman, *J. Chem. Phys.*, 2000, **113**, 9901.
23. G. Fang, J. Zhou, C. Liang, A. Pan, C. Zhang, Y. Tang, X. Tan, J. Liu and S. Liang, *Nano Energy,* 2016, **26**, 57.
24. R. Chen, J. Yao, Q. Gu, S. Smeets, C. Baerlocher, H. Gu, D. Zhu, W. Morris, O. M. Yaghi and H. Wang, *Chem. Commun*., 2013, **49**, 9500.
25. Q. Liu, Z. Low, Y. Feng, S. Leong, Z. Zhong, J. Yao, K. Hapgood and H. Wang, *Micropor. Mesopor. Mat.,* 2014, **194**, 1.
26. O. Komykov. J. -M. Commenge. H. Alem, E. Girot, K. Mozet, G. Medjahdi and R. Schneider, *Mater. Des.,* 2017, **122**, 31.
27. P. Yin, T. Yao, Y. Wu, L. Zheng, Y. Lin, W. Liu, H. Ju, J. Zhu, X. Hong, Z. Deng, G. Zhou, S. Wei and Y. Li, *Angew. Chem. Int. Ed.,* 2016, **55**, 10800.
28. X. He, X. Song, W. Qiao, Z. Li, X. Zhang, S. Yan, W. Zhong and Y. Du, *J. Phys. Chem. C,* 2015, **119**, 9550.
29. B. E. Conway and B. V. Tilak, *Electrochim. Acta*, 2002, **47**, 3571.
30. X. Zhu, X. Shi, A. M. Asiri, Y. Luo and X. Sun, Inorg. Chem. Front., 2018, 5, 1188.
31. W. Chen, J. T. Muckerman and E. Fujita, *Chem. Commun*., 2013, **49**, 8896.
32. Z. Wang, X. Ren, Y. Luo, L. Wang, G. Cui, F. Xie, H. Wang, Y. Xie and X. Sun, *Nanoscale*, 2018, **10**, 12302.
33. J. K. Nørskov, J. Rossmeisl, A. Logadottir, L. Lindqvist, J. R. Kitchin, T. Bligaard and H. Jonsson, *J. Phys. Chem. B,* 2004, **108**, 17886.
34. J. K. Nørskov, T. Bligaard, A. Logadottir, J. R. Kitchin, J. G. Chen, S. Pandelov and U. Stimming, *J. Electrochem. Soc.*, 2005, **152**, J23.
35. S. Zhou, X.W. Yang, W. Pei, N.S. Liu and J.J. Zhao, *Nanoscale,* 2018, **10**, 10876.
36. W. Pei, S. Zhou, Y.Z. Bai and J.J. Zhao, *Carbon,* 2018, **133**, 260.
37. J. K. Nørskov, F. Abild-Pedersen, F. Studt and T. Bligaard, *Proc. Natl. Acad. Sci. U.S.A.,* 2011, **108**, 937.
38. P. T. Wang, X. Zhang, J. Zhang, S. Wan, S. J. Guo, J. L. Yao and X.Huang, *Nat. Commun.,* 2017, **8**, 14580.


 